Journal of Magnetism and Magnetic Materials 438 (2017) 173–180

Contents lists available at ScienceDirect

Journal of Magnetism and Magnetic Materials

journal homepage: www.elsevier.com/locate/jmmm

Adaptable setups for magnetic drug targeting in human muscular arteries: Design and implementation

Amirhossein Hajiaghajani, Soheil Hashemi, Ali Abdolali *

Bioelectromagnetics Group, Applied Electromagnetics Lab, School of Electrical Engineering, Iran University of Science and Technology, Tehran 1684613114, Iran

ARTICLE INFO

Article history:
Received 22 January 2017
Accepted 22 April 2017
Available online 2 May 2017

Keywords:
Magnetic targeting
Drug delivery
Muscular vessel
Particle tracing
In-vitro validation

ABSTRACT

Magnetic drug targeting has been used to steer magnetic therapeutic agents and has received much attention for capillaries and human brain arteries. In this paper, we focus on noninvasive targeting of nanoparticles in muscular arteries, in where the vessel diameter and blood flow are much challengingly higher than brain capillaries. We aim to design a low intensity magnetic field which avoids potential side effects on blood cells while steers particles with high targeting rate. The setup design procedure is considerably flexible to be used in a wide variety of large vessels. Using particle tracing, a new method is proposed to connect the geometry of the vessel under the action of targeting to the required magnetic force. Specifications of the coil which is placed outside the body are derived based on this required force. Mutual effects of coil dimensions on the produced magnetic force are elaborated and summarized in a design flowchart to be used for arbitrary muscular vessel sizes. The performance of the optimized coil is validated by *in vitro* experiments and it is shown that particles are steered with the average efficiency of 80.2% for various conditions.

1. Introduction

Noninvasive magnetic drug targeting has been used as an approach to transport therapeutic agents attached to magnetic carriers to disease regions such as tumors by the use of magnetic fields created by external magnets or coils [1–9]. This technique eliminates the excess use of drugs, radionuclide or genes those lead to side effects such as hair loss, fatigue, mouth and throat sores [10,11]. In previous works permanent magnets have been used to create the magnetic field (H) in a target vessel branch where with forming and placing magnets, a gradient H was created [8,9,12–14]. Nowadays, using electromagnets (such as coils) is conventional which enables us to spatially form the magnetic field [15,16]. The magnetic targeting issue has received much attention specially to microvessels such as brain capillaries unlike the large-sized muscular arteries.

Muscular arteries have three major geometric differences with capillaries. First, they are commonly located deeper inside the human body (where the deepness would reach to 5 cm) than shallow microvessels. Second, they include millimeter-sized vessels with a lumen diameter up to 6 mm unlike microvessels such as arterioles and capillaries with the lumen diameter from 5 to 20 μm. Third, they possess much higher blood velocity compared to capillaries [17]. Accordingly, some considerations brought up in design methods of electromagnets for muscular vessels. First, one cannot place the coil very close to the vessel under targeting, because the vessel is surrounded by muscle and skin. Many studies have been done in order to cover the magnetic targeting problem in brain vessels and shallow capillaries close to the skin surface where the depth was averagely supposed 3 mm [15,18–20]. Though implantation of magnets and metal lines close to the deep vessels shows high efficiency, it is not categorized in noninvasive treatment [21–24].

In microvessels, the no-slip boundary condition reduces the near-wall blood velocity relative to the centerline [25] and improves the ability of catching particles by weaker magnetic force due to much lower drag compared to millimeter vessels. In this situation the required H intensity is far lower than the maximum permissible exposure [3,26–29]. However, due to higher blood flow rate in muscular vessels, particles need higher magnetic force (and thus stronger H) to be steered against the tough drag force which is produced in the opposed direction of particle movement. It is known that the exposure of an intense H can create unexpected side effects on human body and blood cells. Hence, the second issue in magnetic targeting is the limitation on the applying H, imposed by the maximum permissible exposure (up to 0.28 MA/m) for the human body in a controllable environment in subject to [30] which becomes important for muscular arteries. Also, a simple coil which produces an intense H consumes high current and

* Corresponding author.
E-mail address: abdolali@iust.ac.ir (A. Abdolali).

http://dx.doi.org/10.1016/j.jmmm.2017.04.058
0304-8853/

causes extra heat and eventually may destruct the coil wire shield and cause damage to patient's outer tissue. Thus, by considering the limitation of coil current, the coil design must be changed so that it reaches the lowest conductivity loss while producing the highest available magnetic force, and eliminates the need for high amperage supply for magnetic targeting in muscular vessels.

The most challenging issue in steering of magnetic drugs is that the magnetic force is in proportion with the particle's volume while drag scales by its radius, thus we expect a lower particle guidance rate for smaller nanoparticles. However, high guidance rate had been shown both for *in vitro* and *in vivo* experiments [4,19,31–33]. This was justified by aggregation of single particles and formation of super particles [7]. The magnetic Richardson number (the ratio of the magnetic force to the Stokes drag force at the centerline of a blood vessel [34]) for super particles is much higher than singles.

The optimization of coil specifications depends on the blood vessel geometry held below the coil. For example, consider two patients who have tumors in their breast and kidney. Their cardiovascular geometries between the drug injection point and the tumor are different, but can be divided into the same Y-shaped junctions with various geometries. Therefore, the coil must be designed for the corresponding Y-junction or equally, an optimization goal must be defined as a function of the vessel geometry. The general geometry of Y-shaped junction which has been often considered in the literature enables us to model the injection-tumor path by a few isolated junctions [8,25,35,36]. Fig. 1 depicts a schematic model of this path.

In this paper, we suppose super particles with an effective radius that is larger than single particles radius and predict the required magnetic force under which particles are guided successfully. This includes particle tracing in Y-junctions with much higher blood flow velocity relative to previous studies and can cover the muscular arteries situation that received low attention in magnetic drug targeting literature. We connect the required magnetic force to the coil to map the required magnetic force to the coil dimensions and specification. In addition, numerical simulations have been performed in COMSOL environment (the commercially available software using finite element method) to distinguish the effects of structural parameters of the coil on the spatial form of magnetic force applying to a reference particle in an arbitrary muscular artery. The proposed algorithm can be used flexibly for user defined vessels with different geometries. The proposed setup based on this method is simple to use, easy to install and efficient while covering many types of arteries and aortas.

2. Muscular vessel modeling

In this section we develop the physical model to find the required magnetic force which would be used to design the coil. In numerous studies, physical models were introduced in which the dominant forces were the Stokes drag, magnetic, advection and diffusion (Brownian and interaction of particles with blood cells) [25,33,37–42]. In some previous works, it was shown that the Brownian diffusion does not change the particle trajectory unlike drag and magnetic forces [15,43,44]. Our model uses magnetophoresis and drag forces to predict the particle trajectory, because they are much stronger than other forces inside a muscular artery [4,15,25,44]. This study focuses on particle tracing rather than its absorption by the walls, because the absorption stage occurs in capillaries with lower blood flow after the targeting action.

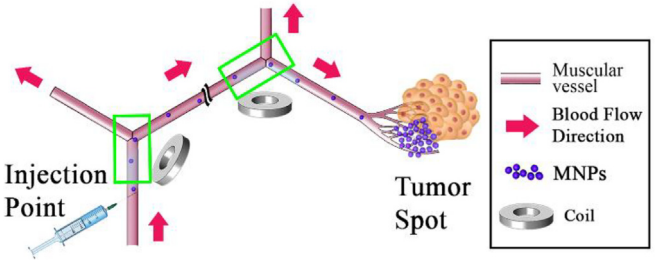

Fig. 1. Schematic of magnetic nanoparticle (MNP) trajectory in the presence of magnetic force for human muscular vessels. Isolated coils are placed outside the patient's body for nondestructive treatment.

The magnetophoretic force that can be derived by Maxwell equations, is given by [45]

$$\vec{F}_{MP} = \mu_f \vec{M} \cdot \vec{\nabla} H \tag{1}$$

where $\vec{M}$ and μ_f indicate the effective magnetic moment of spherical particles and fluid permeability, respectively. In the case of saturation, $\vec{M}$ would change to the saturated magnetic moment ($\vec{M}_{sat}$). Instead, while particles are not magnetically saturated, (1) can be written as [45]

$$\vec{F}_{MP} = 2\pi\mu_f r_p^3 \frac{\mu_p - \mu_f}{\mu_p + 2\mu_f} \vec{\nabla} H^2 \tag{2}$$

where r_p and μ_p are spherical particle radius and permeability, respectively. The Clausius–Mossotti ratio ($\frac{\mu_p-\mu_f}{\mu_p+2\mu_f}$) is near unity, because of the high particle permeability relative to the blood. Although the amplitude of H decreases in the deep vessels [46], the spatial form of DC or extremely low frequency H does not change while penetrating into the body because tissues are comprised of nonmagnetic materials.

As a result of symmetric stress tensor and being an isotropic fluid, blood is considered a Newtonian fluid [47–49]. Also, this assumption holds true in the blood vessels with a diameter larger than 100 μm [50]. The Stokes drag force is derived from [45]

$$\vec{F}_D = 6\pi\eta r_p (\vec{v}_f - \vec{v}_p) \tag{3}$$

where η, v_f, and v_p are dynamic viscosity of blood (3 mPa·s), fluid velocity (constant over time) and particle velocity (as a function of time), respectively.

In our Y-shaped junction model (depicted in Fig. 2) the main vessel includes only the x component (We shall refer to the x and z component of a vector throughout this work by the index of x

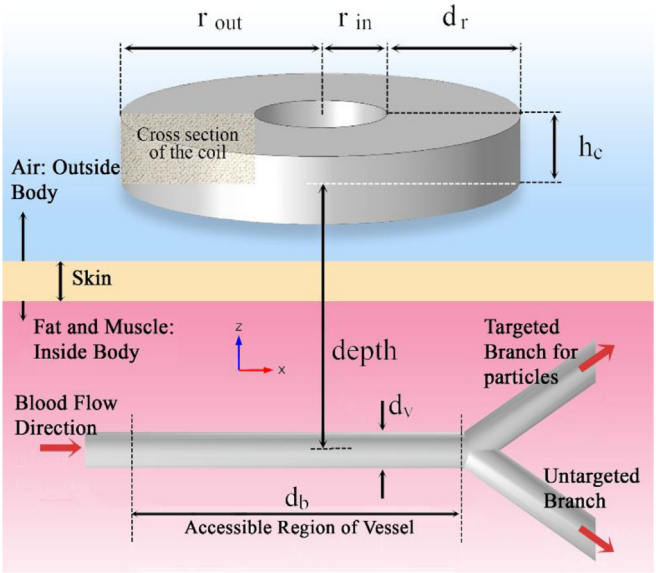

Fig. 2. Geometry of coil and blood vessel. All regions are nonmagnetic materials.

and z, respectively). Across the available targeting distance below the coil (d_b), the vessel centerline has only the x component ($v_{f_y} = v_{f_z} = 0$). We consider the slip boundary condition for muscular vessel walls due to their uniform blood flow profile (v_{f_x} is constant over z axis) [22,51].

According to Newton's 2nd law of motion, the movement of the particles is derived from

$$\vec{F}_{MP} + \vec{F}_D = m_p \frac{d\vec{v}_p}{dt} \tag{4}$$

where m_p is the particle mass. By solving (4) for $\vec{v}_p$ we find

$$\vec{v}_p(t) = \vec{v}_f + \frac{\vec{F}_{MP}}{6\pi\eta r_p} \times \left(1 - \exp\left(-\frac{6\pi\eta r_p}{m_p} t\right)\right) \tag{5}$$

On the x direction, we can assume a constant particle velocity equal to blood velocity, because the magnetic force is much weaker than drag. Therefore, the time taken by particles to move along the distance d_b is

$$\Delta t_x = \frac{d_b}{v_{f_x}} \tag{6}$$

To affect the impact of super particle formation which was seen in previous *in vivo* and *in vitro* experiments [7], we replace r_p (single particle) with effective r_c (cluster of particles). We have assumed the clusters to be small enough to not block the blood flow. As a physical interpretation, this would add the particle-particle diffusion effect to the model. The term $\tau_c = m_c/(6\pi\eta r_c) = 2\rho_p r_c^2/(9\eta)$ indicates the time constant which leads particles to move in the z direction (see Fig. 2). In z axis (5) reduces to

$$v_{c_z}(t) \cong \frac{F_{MP_z}}{6\pi\eta r_c} \times \left(1 - \exp\left(-\frac{9\eta}{2\rho_p r_c^2} t\right)\right) \tag{7}$$

If the cluster effective radius is large enough so that $5\tau_c$ (the time that the exponential term is approximately nonzero) would be in the order of Δt_x, the velocity change can be sensed and clusters move with acceleration. Else, if $5\tau_c \ll \Delta t_x$, the near-zero exponential term leads to a constant velocity movement.

Thus, two types of movement can be seen in the z direction. First, the constant velocity ($v_{c_z} = F_{MP_z}/6\pi\eta r_c$) for smaller clusters, where the time it takes to raise clusters from down to top of the vessel (the longest path for successive steering) can be calculated by

$$\Delta t_z = d_v / \left(\frac{F_{MP_z}}{6\pi\eta r_c}\right) \tag{8a}$$

Second, for the movement with a constant acceleration ($a_{c_z} = F_{MP_z}/m_c$) for larger clusters the raising time changes to

$$\Delta t_z = \sqrt{\frac{2d_v}{F_{MP_z}/m_c}} \tag{8b}$$

For two movement types (8a) and (8b) concludes the required magnetic force for steering

$$F_{MP_z} = \frac{24Q\eta r_c}{d_b d_v}; \text{(non-accelerated)} \tag{9a}$$

$$F_{MP_z} = \frac{128Q^2\rho_p r_c^3}{3\pi d_b^2 d_v^3}; \text{(accelerated)} \tag{9b}$$

where Q is the blood flow rate ($Q = \pi d_v^2 v_{f_x}/4$). From (5) to (10) a uniform spatial form for F_{MP_z} has been considered in the interval of x from 0 to d_b. To compare produced magnetic forces, we divide F_{MP_z} by r_c^3 to get the normalized magnetic force denoted by index n throughout this paper. COMSOL Multiphysics simulations show the Gaussian spatial distribution of $F_{MP_{nz}}$ versus x axis on the vessel centerline for various coils, as shown in Fig. 3c for a typical coil.

As shown in Fig. 3, the produced F_{MP_z} is actually a Gaussian function of observation point (x). The effective time in which a cluster senses the magnetic force is shorter for Gaussian distribution relative to uniform. Thus, to compensate the difference between the cluster movement under these two distributions and equalize the cluster movement in the z direction, the required *force factor* in uniform distribution is multiplied by the correction factor (*CF*; a number larger than unity). We define a scalar parameter by integrating $F_{MP_{nz}}$ over x axis in this interval. This is to numerically compare the produced magnetic force by different coils on a normalized cluster size. We define the scalar *force factor* by

$$F_{I_{zn}}(x) = CF \times \int_0^{d_b} \frac{F_{MP_z}}{r_c^3} dx \cong CF \times F_{MP_z} \times \frac{d_b}{r_c^3} \ (\mathrm{N/m^2}) \tag{10}$$

where by multiplying the *CF*, the F_{MP_z} is assumed to have a uniform distribution over the x interval of 0 to d_b. This factor would be used for optimization of the coil. We connect the magnetic force to vessel geometry by this parameter. The model proposed here is developed in MATLAB to calculate the particle trajectory. The *CF* has been adjusted so that the cluster movements for both spatial distributions match together. We find that this goal is reached for various clusters and vessel geometries at the *CF* equal to 3.20. Fig. 4 shows the particle tracing results for the proposed physical model.

3. Design procedure of the setup and discussion

After the calculation of *force factor* in the previous section, here we describe its realization. Our proposed setup consists of one cylindrical coil with a magnetic core supplied by a DC voltage source to control the cluster movement in the vessel under test.

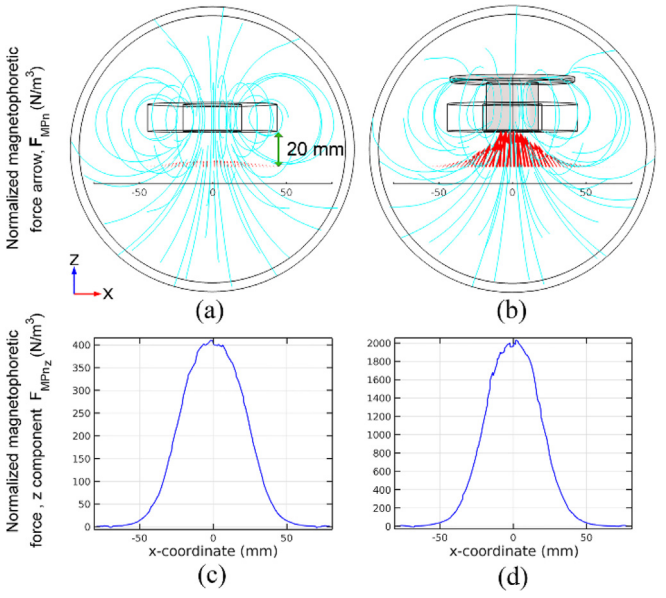

Fig. 3. Deriving normalized spatial form of magnetic force in 20 mm below the coil and voltage supply of 1 V. (a): a typical coil without core. (b): effect of the proposed core. Magnetophoretic force vectors are plotted in red and with the same scale factors (c): the normalized magnetic force spatial form of a typical coil without core. (d): the normalized magnetic force spatial form of the same coil with magnetic core made from steel ST37.

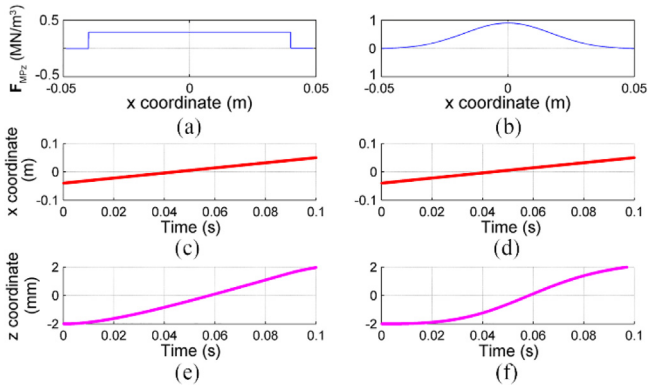

Fig. 4. Trajectory of clusters with the effective radius of 10 μm while applying the correction factor in a vessel diameter of 4 mm. Left column is the uniform distribution of magnetic force while the right column is the Gaussian spatial form of a typical coil. a, b: the *z* component of different normalized force distributions along *x* axis. The *x* component of the magnetic force is much smaller than the *z* component and is neglected. c, d: the *x* direction movement under the magnetic and drag forces. e, f: equal *z* direction movements under different spatial distributions of magnetic force.

The structural parameters of the coil are the inner radius (r_{in}), outer radius (r_{out}), differential radius (d_r), height of the coil (h_c), wire diameter (d_w), specific resistance of the wire (ρ_{cu}), depth between the coil and the centerline of the vessel (*depth*), voltage supply (V_S), number of turns of the coil (N), particle permeability (μ_p), blood permeability (μ_f) and core dimensions. Geometric parameters of the vessel include its diameter (d_v) and the accessible distance where the coil is placed above it (d_b) as shown in Fig. 2. Based on the Biot-Savart formula [52], we conclude that the *depth*, supplying voltage and the core effect have no mutual impact on the *force factor*. However, *force factor* is affected by d_r, h_c and d_w mutually [15]. We find that the wire shield and air gaps add 60 μm to the wire diameter. For a typical coil the number of turns can be approximated by

$$N = \left\lfloor \frac{d_r}{d_w + 60\ \mu\text{m}} \right\rfloor \times \left\lfloor \frac{h_c}{d_w + 60\ \mu\text{m}} \right\rfloor \tag{11}$$

This shows that coil dimensions determine the wire length, which is in proportion to the total resistance. Conventional power supplies are actually voltage sources; thus, the wire resistance plays a key role in optimizing the consumed power of the coil. The terminal resistance of the coil wire is derived from

$$R_{coil} = \rho_{Cu} \frac{l}{0.25\pi d_w^2} \tag{12}$$

where ρ_{cu} and l are the specific resistance of the copper and the wire length, respectively. The total wire length is calculated using the summation

$$l = 2\pi\left(r_{in} + (r_{in}+d_w) + (r_{in}+2d_w) + \ldots + (r_{in}+d_r)\right) \times \left\lfloor \frac{h_c}{d_w} \right\rfloor = \\ = \frac{2\pi h_c}{d_w}\left(\sum_{n=0}^{\lfloor d_r/d_w \rfloor} r_{in} + nd_w\right) \cong N \times 2\pi\left(r_{in} + \frac{\lfloor d_r/d_w \rfloor d_w}{2}\right) \cong N \times 2\pi\left(r_{in} + \frac{d_r}{2}\right) \tag{13}$$

Consequently, the coil current would be calculated by the Ohm's law. Note that a cylindrical coil with current I is unequal to a single loop with current NI, because a multiturn coil is comprised of N loops which are placed in different positions. The AC/DC physics of COMSOL Multiphysics is used to simulate the effect of structural parameters of the coil on the produced *force factor*. In our simulation model, the cross section of the coil is divided into N loops. The calculated total resistance by (12) with the use of (13) has been considered for the coil. To steer particles successfully, the setup must exert an equal or stronger *force factor* relative to the required one described in the previous section. Here, the effects of coil parameters are discussed.

3.1. Inner and outer radius (r_{in}, r_{out})

Simulation of various coils shows that the *force factor* does not vary much for r_{in} from 15 to 20 mm due to spatial integration of magnetic force according to (10). To reduce the complexity of design procedure, we set r_{in} = 17 mm for all coils.

The coil must be placed above the targeting region (d_b) so that the outer radius would not exceed the distance d_b

$$2(r_{in} + d_r) \leqslant d_b \tag{14}$$

Therefore, the spatial interval of the applying magnetic force is confined from x = 0 to d_b.

3.2. Height of the coil (h_c) and wire diameter (d_w)

As d_r has been determined before, the effect of h_c and d_w would be selected together. The wire diameter makes a tradeoff between the consumed power and reaching to the maximum *force factor*. According to (11) for a unique cross section area of the coil (depicted in Fig. 2) and voltage, reduction of d_w consequences in increasing the N and coil resistivity, and decreasing the sunk current (or vice versa). Various combinations of coil dimensions and wire diameter are simulated and results are shown in Fig. 5. It is shown that by moving along the curve $d_r \times h_c$ = cte (specific cross section area), the *force factor* stays approximately fixed. The interval of d_r in which the maximum *force factor* occurs is highlighted in Fig. 5.

This means h_c and d_r have a coupled effect on maximizing the *force factor* and can be used to find the commensurate d_w based on the d_r. Although the Ampere-turn grows by increasing d_w, it is impractical to use a very thick wire for small d_r because it needs a very high current source as its feed. In addition, magnetic force simulations show this growth stops for $d_w > 0.7$ (see Fig. 6); because at this point, the effect of decreasing the number of turns dominates the effect of low coil resistivity.

3.3. Distance from coil to vessel (depth)

The magnetic field intensity and thus the *force factor* drop by increasing the distance from the coil to the vessel. Consider an equivalent circular loop located in plane $z = z_0$ with the radius of R. Along its centerline (curve $x = y = 0$), the magnetic field on a vessel placed on the curve $y = z = 0$ [53] and *force factor* can be written as

$$H = \frac{IR^2}{2} \frac{1}{\left(R^2 + z_0^2\right)^{1.5}} \tag{15a}$$

$$F_{l_z} \propto \frac{\partial}{\partial z} H^2 \propto \frac{z_0}{\left(R^2 + z_0^2\right)^3} \tag{15b}$$

While this equivalent loop is placed in the center of the coil's cross section (or equivocally with the effective radius of $R = r_{in} + d_r/2$ in plane $z_0 = depth + h_c/2$) the COMSOL simulation matches to (15b), (see Fig. 7).

To convert the produced *force factor* from the depth of 20 mm (as shown in Fig. 3 and 5) to an arbitrary depth of h_0, we use the ratio of *force factor* in the new depth to the *force factor* in the 20 mm depth

$$F_{l_z}(h_0) = F_{l_z}(20\,[\text{mm}]) \times \frac{\left(h_0 + \frac{h_c}{2}\right)}{\left(\left(r_{in} + \frac{d_r}{2}\right)^2 + \left(h_0 + \frac{h_c}{2}\right)^2\right)^3} \Big/ \frac{\left(20\,[\text{mm}] + \frac{h_c}{2}\right)}{\left(\left(r_{in} + \frac{d_r}{2}\right)^2 + \left(20\,[\text{mm}] + \frac{h_c}{2}\right)^2\right)^3} \tag{16}$$

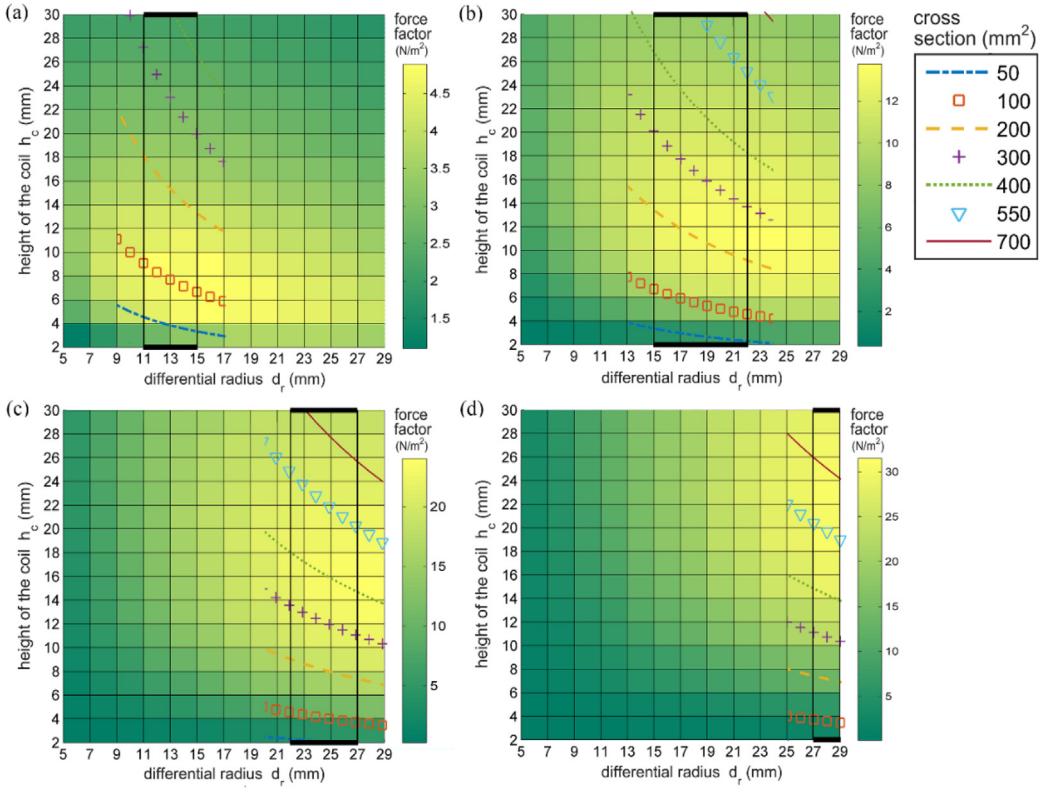

Fig. 5. *Force factor* versus d_r and h_c for various wire diameters in 20 mm below the coil and voltage supply of 1 V. d_r intervals where the *force factor* reaches to its maximum is highlighted by bold lines (a) for $11 < d_r < 15$, $d_w = 0.3$ mm (b) for $15 < d_r < 22$, $d_w = 0.45$ mm (c) for $22 < d_r < 27$, $d_w = 0.6$ mm (d) for $27 < d_r$, $d_w = 0.75$ mm. Various cross section areas are plotted by the curves $d_r \times h_c = cte$.

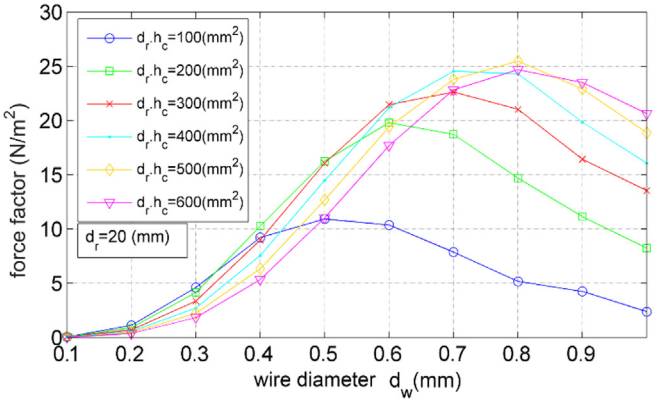

Fig. 6. Effect of wire diameter on the *force factor* for various cross section areas. It is seen that the increase of *force factor* peak stops for d_w greater than 0.7 mm, therefore larger d_w would not increase the *force factor* because of the reduced number of turns in the coil. This figure is prepared for $d_r = 20$ mm and shows the stop point of d_w (0.7 mm), which would change for a different d_r.

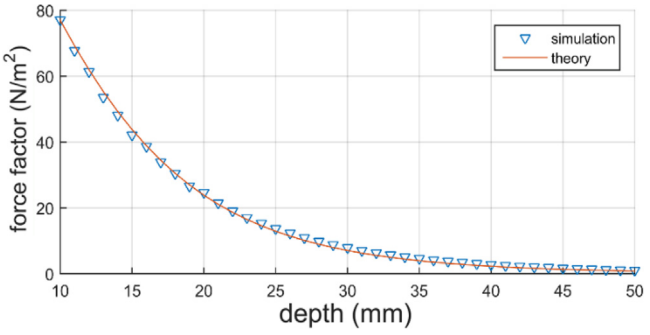

Fig. 7. The effect of depth on the *force factor* by simulation for a cylindrical multiturn coil (supplied by 1 V) and a theoretical equivalent single loop placed in the center of the cross section of the coil.

3.4. Steel core and terminal voltage of the coil (V_S)

Regarding (2) and the vector factorization $\vec{\nabla} H^2 = 2(\vec{H}\cdot\vec{\nabla})\vec{H}$, the magnetophoretic force is proportional with both magnetic field intensity and its gradient. To compensate the limitation on H intensity, a high gradient H is created by a magnetic core. It strengthens the *force factor*, because the high permeability of the core (μ_{core}) decreases the magnetic resistance of the H path; also, this high permeability contrast creates a high gradient H near the core boundary. We insert a cylindrical core with the radius of 16 mm aligned with the bottom of the coil. To reduce the magnetic resistance of the coil, we placed a disk geometry on top of the core. In low voltage when the core is not saturated, we find from (2) that

$$F_{I_z} \propto \mu_{core} V_S^2 \tag{17}$$

Generally, μ_{core} is a function of H and for a typical muscular vessel, the required H is often strong enough to saturate the core. We have used the permeability profile of commercial steel ST37 in the simulations. It is seen that for different coil structures, regarding the core saturation, a cylindrical core with a height equal to h_c and a disk with a radius equal to r_{out}, creates the largest *force factor* (4.9 times more than when no core is inserted). The spatial form of magnetic force while using the core is depicted in Fig. 3b. According to (2) to calculate the required voltage supply we use

$$V_S = \sqrt{F_{I_z}^{\ required} / F_{I_z}^{(V_S=1)}} \tag{18}$$

where $F_{l_z}^{required}$ has been calculated from (10) and $F_{l_z}^{(V_S=1)}$ is the produced *force factor* up to this point by 1 V supply, with designed dimensions, magnetic core and for the desired depth.

3.5. Design procedure flowchart

The design procedure of the proposed setup for magnetic drug targeting in human muscular vessels is proposed as shown in Fig. 8. The coil designed for common human muscular vessels by this method, produces an H with much lower intensity than the maximum tolerable amount of DC magnetic exposure under controlled environment for the human body [30].

4. *In-vitro* validation

To validate the proposed physical model and setup, we use silicone pipe with the inner diameter of 4 mm as well as a typical muscular artery. Normal blood flow velocity in human muscular arteries, ending to the kidney, head and liver are 0.55, 0.75 and 1.1 L/min, respectively [25,54]. Iron particles have been used for *in vitro* and *in vivo* in previous experiments. The injected iron particles were reported to have no side effect in rats and human (up to 2.6 mg) [55,56]. Here we use iron particles with the permeability of $\mu_p \cong 1000\mu_0$, average radius of 700 nm, measured by dynamic light scattering and density of 7.028 g/cm^3. Also, d_b is assumed 80 mm because it is close to the minimum distance between two sequential blood vessel branches from a main muscular vessel where is accessible for targeting action. The carrier solution is made by dissolving 30% Wt. glycerol in water to make the blood replacement solution with a dynamic viscosity close to blood in the room temperature [57]. The cluster radius of 130 μm is measured while floating in the solution by small angle X-ray scattering. A comparison between 5τ and Δt_x subject to (6) and (7) shows that clusters move along the z direction with acceleration; thus, using (9b) and (10), the required *force factor* for the blood flowrate of 0.857 L min^{-1} is calculated 12,239 N/m^2. Based on the designing flowchart, by the use of Fig. 5, we find d_r = 23 mm. For this range of d_r, we choose d_w = 0.6 mm in where the maximum *force factor* occurs at h_c = 18 mm. By this combination, the initial produced *force factor* with unit voltage and a *depth* of 20 mm is 22 N/m^2.

We perform the test for depth of 10, 15 and 20 mm, thus based on (16), the initial *force factor* multiplies by 3.31, 1.87 and 1 to

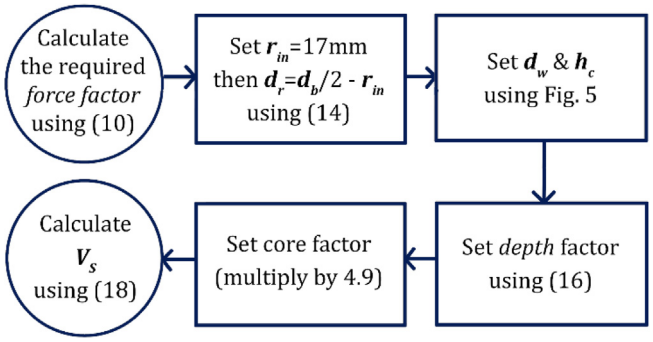

Fig. 8. Design procedure flowchart.

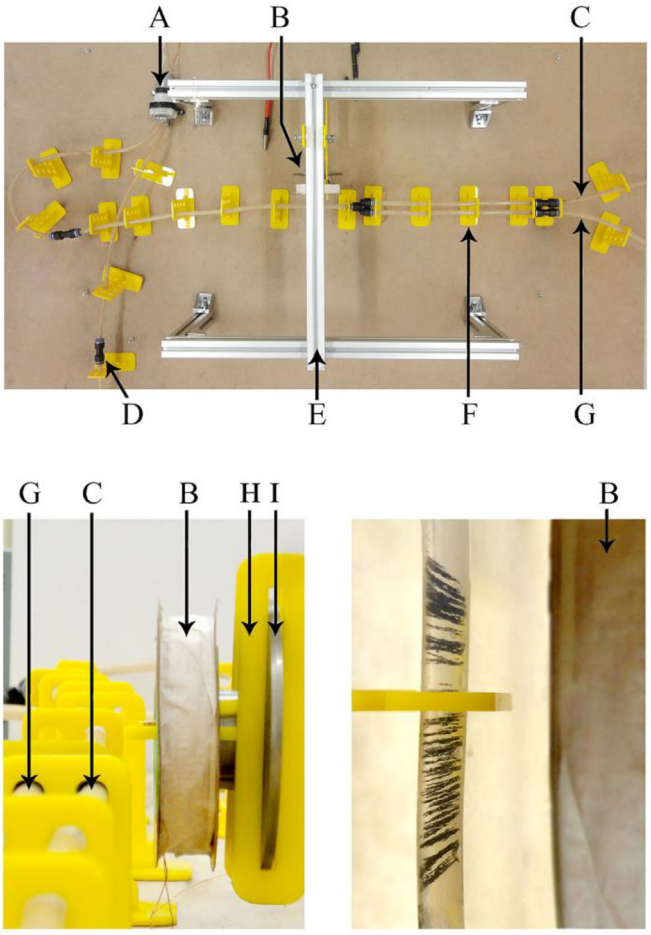

Fig. 9. Our *in vitro* test setup. Formation of particle clusters while applying a magnetic field with a zero flow rate is seen. Appliances: A. controlled fluid pump. B. The coil. C. Targeted branch. D. Particles inlet. E. Aluminum fixture. F. Plastic pipe fixture. G. Untargeted branch. H. Core plastic fixture. I. Steel core.

Table 1
Results of *in vitro* test for various depths and fluid flows. For this experiment 5τ = 8.8 ms is in the order of Δt_x. Accordingly, particles move along the z direction with acceleration. Selected flow rates are close to natural blood flow in human muscular arteries. The average successful guidance percentage is 80.2%.

Test #	*Depth* (mm)	Q (L/min)	Δt_x (s)	Calculated & applied V_S (V)	*SGP* (%)
1	10	0.857	0.070	9.0	79.3
2	10	1.034	0.058	10.9	81.0
3	10	1.111	0.054	11.7	79.8
4	10	1.154	0.052	12.1	81.2
5	15	0.857	0.070	12.0	81.6
6	15	1.034	0.058	14.5	80.5
7	15	1.111	0.054	15.5	82.5
8	15	1.154	0.052	16.1	82.5
9	20	0.857	0.070	16.4	79.6
10	20	1.034	0.058	19.8	77.1
11	20	1.111	0.054	21.2	77.9
12	20	1.154	0.052	22.0	80.0

Table 2
results of *in vitro* test while the applied voltages changed ±20% from the calculated voltage. The *SGP* shows that the calculated voltage is at its optimum point.

Test #	*Depth* (mm)	*Q* (L/min)	Δt_x (s)	Applied V_S (V)	*SGP* (%)
13	10	0.857	0.070	10.8	84.6
14	10	1.034	0.058	13.1	83.5
15	10	1.111	0.054	14.0	84.5
16	10	1.154	0.052	14.5	82.5
17	10	0.857	0.070	7.2	64.3
18	10	1.034	0.058	8.7	69.0
19	10	1.111	0.054	9.4	70.8
20	10	1.154	0.052	9.7	66.2

reach 356.9, 201.1 and 107.8, respectively. The coil under test comprises of 930 turns of insulated wire with the measured terminal resistance of 10.5 Ω and is fed by a DC voltage supply. Also, a DC water pump and flow control valves are used to adjust the precise flow rate (as listed in Table 1). The fluid flow in two targeted and untargeted branches is kept equal. Pipes, the coil and its core are fixed by nonmagnetic plastic fixtures. While performing the test, the mixture of fluid and particles is kept homogeneous in the input chamber of the pump.

After performing each test with different parameters, two separate mixtures of targeted and untargeted branches are accumulated and dried. The mass of each sample is measured using an electronic scale with the precision of 0.001 g. The test setup and used materials are located in Fig. 9.

For each combination of parameters, a separate test is performed. The voltage is applied to terminal of the coil with the precision of 0.1 V. We define the successful particle guidance (*SPG*) as the mass fraction of steered particles to the sum of steered and non-steered particles. The average SPG percentage for various depths and fluid flows is 80.2% (as shown in Table 1).

To check the optimized voltage, tests no. 1 to 4 are repeated with 20% fluctuation in voltage V_S, and new *SGP*s are listed in Table 2 (tests no. 13–16 and 17–20, respectively). Averagely by raising the voltage, the *SPG* increases by 1.94%, which stays at an approximately constant value; while for the fallen voltage, it decreases by 14.26%. This demonstrates the optimized calculated voltage in (10).

5. Conclusion

The physical model of magnetic drug delivery is simplified in muscular vessels by neglecting the diffusive force and instead, using an effective radius of particle clusters in computations. We first proposed a method for calculation of required magnetic force and second, the design algorithm of that force is put forward by elaborating the mutual effect of coil specifications on the produced magnetic force. This can be used to adjust coil dimensions to fit and optimize it for the correspond vessel. Optimization means creating the most effective magnetic force with a lower *H* intensity which passes the maximum permissible magnetic exposure to the human body. Coil dimensions and the wire diameter show mutual effects on the created magnetic field which were discussed. There is a tradeoff between the low ampere-turn and low terminal resistance of the coil to reach the optimum power consuming coil. A magnetic cylindrical core with a disk placed above it, improved the magnetic force by 4.9X. Experimental *in vitro* test shows that nanoparticles also are steered by coils supplied with low current sources while they form super particles. The experimentally validation of optimized results approved the slip boundary condition and the plug flow profile considered for millimeter sized muscular vessels in the proposed model. This method can generally be used for user defined vessel geometries with high diameter and blood velocity. Also, as low power voltage sources are easy to be afforded, this method eases the use of magnetic drug delivery for local clinics.

Acknowledgements

This research did not receive any specific grant from funding agencies in the public, commercial, or not-for-profit sectors.

References

[1] A. Sarwar, A. Nemirovski, B. Shapiro, Optimal Halbach permanent magnet designs for maximally pulling and pushing nanoparticles, J. Magn. Magn. Mater. 324 (2012) 742–754, http://dx.doi.org/10.1016/j.jmmm.2011.09.008.
[2] L.C. Barnsley, D. Carugo, J. Owen, E. Stride, Halbach arrays consisting of cubic elements optimised for high field gradients in magnetic drug targeting applications, Phys. Med. Biol. 60 (2015) 8303–8327, http://dx.doi.org/10.1088/0031-9155/60/21/8303.
[3] Q. Cao, X. Han, L. Li, Numerical analysis of magnetic nanoparticle transport in microfluidic systems under the influence of permanent magnets, J. Phys. D Appl. Phys. 45 (2012) 465001, http://dx.doi.org/10.1088/0022-3727/45/46/465001.
[4] H. Xu, T. Song, X. Bao, L. Hu, Site-directed research of magnetic nanoparticles in magnetic drug targeting, J. Magn. Magn. Mater. 293 (2005) 514–519, http://dx.doi.org/10.1016/j.jmmm.2005.01.067.
[5] S. Nishijima, F. Mishima, T. Terada, S. Takeda, A study on magnetically targeted drug delivery system using superconducting magnet, Phys. C Supercond. Appl. 463–465 (2007) 1311–1314, http://dx.doi.org/10.1016/j.physc.2007.03.493.
[6] M. Dadkhah, N. Kumar, J. Yoon, Design and simulation of a 3D actuation system for magnetic nano-particles delivery system, Lect. Notes Comput. Sci. (Including Subser. Lect. Notes Artif. Intell. Lect. Notes Bioinformatics). 8102 LNAI (2013) 177–187, http://dx.doi.org/10.1007/978-3-642-40852-6-20.
[7] A. Nacev, C. Beni, O. Bruno, B. Shapiro, The behaviors of ferromagnetic nanoparticles in and around blood vessels under applied magnetic fields, J. Magn. Magn. Mater. 323 (2011) 651–668, http://dx.doi.org/10.1016/j.jmmm.2010.09.008.
[8] K. Gitter, S. Odenbach, Investigations on a branched tube model in magnetic drug targeting-systematic measurements and simulation, IEEE Trans. Magn. 49 (2013) 343–348, http://dx.doi.org/10.1109/TMAG.2012.2224324.
[9] K. Gitter, S. Odenbach, Quantitative targeting maps based on experimental investigations for a branched tube model in magnetic drug targeting, J. Magn. Magn. Mater. 323 (2011) 3038–3042, http://dx.doi.org/10.1016/j.jmmm.2011.06.055.
[10] F. Qiu, S. Fujita, R. Mhanna, L. Zhang, B.R. Simona, B.J. Nelson, Magnetic helical microswimmers functionalized with lipoplexes for targeted gene delivery, Adv. Funct. Mater. 25 (2015) 1666–1671, http://dx.doi.org/10.1002/adfm.201403891.
[11] K.M. Krishnan, Fundamentals and Applications of Magnetic Materials, Oxford Univ Press, 2016.
[12] Z.G. Forbes, B.B. Yellen, K.A. Barbee, G. Friedman, An approach to targeted drug delivery based on uniform magnetic fields, Magn. IEEE Trans. 39 (2003) 3372–3377, http://dx.doi.org/10.1109/TMAG.2003.816260.
[13] J. Lunacek, M. Lesnak, P. Jandacka, R. Dvorsky, J. Repkova, J. Seidlerova, N. Vitkovska, Efficiency of HIGH gradient magnetic separation applied to micrometric magnetic particles, Sep. Sci. Technol. 6395 (2015), http://dx.doi.org/10.1080/01496395.2015.1061006, 150701140517004.
[14] J.A. Ritter, A.D. Ebner, K.D. Daniel, K.L. Stewart, Application of high gradient magnetic separation principles to magnetic drug targeting, J. Magn. Magn. Mater. 280 (2004) 184–201, http://dx.doi.org/10.1016/j.jmmm.2004.03.012.
[15] M.D. Tehrani, M.O. Kim, J. Yoon, A novel electromagnetic actuation system for magnetic nanoparticle guidance in blood vessels, IEEE Trans. Magn. 50 (2014) 1–12, http://dx.doi.org/10.1109/TMAG.2014.2307271.
[16] B. Gleich, N. Hellwig, H. Bridell, R. Jurgons, C. Seliger, C. Alexiou, B. Wolf, T. Weyh, Design and evaluation of magnetic fields for nanoparticle drug targeting in cancer, IEEE Trans. Nanotechnol. 6 (2007) 164–169, http://dx.doi.org/10.1109/TNANO.2007.891829.
[17] P.I. Aaronson, J.P.T. Ward, M.J. Connolly, A. Fallis, The Cardiovascular System at a Glance, John Wiley & Sons, 2013, http://dx.doi.org/10.1017/CBO9781107415324.004.
[18] A.S. Lübbe, C. Alexiou, C. Bergemann, A.S. Lubbe, Clinical applications of magnetic drug targeting, J. Surg. Res. 95 (2001) 200–206, http://dx.doi.org/10.1006/jsre.2000.6030.
[19] R. Ganguly, A.P. Gaind, S. Sen, I.K. Puri, Analyzing ferrofluid transport for magnetic drug targeting, J. Magn. Magn. Mater. 289 (2005) 331–334, http://dx.doi.org/10.1016/j.jmmm.2004.11.094.
[20] P. Dames, B. Gleich, A. Flemmer, K. Hajek, N. Seidl, F. Wiekhorst, D. Eberbeck, I. Bittmann, C. Bergemann, T. Weyh, L. Trahms, J. Rosenecker, C. Rudolph, Targeted delivery of magnetic aerosol droplets to the lung, Nat. Nanotechnol. 2 (2007) 495–499, http://dx.doi.org/10.1038/nnano.2007.217.
[21] M.O. Avilés, H. Chen, A.D. Ebner, A.J. Rosengart, M.D. Kaminski, J.A. Ritter, In vitro study of ferromagnetic stents for implant assisted-magnetic drug targeting, J. Magn. Magn. Mater. 311 (2007) 306–311, http://dx.doi.org/10.1016/j.jmmm.2006.11.156.

[22] M.O. Avilés, A.D. Ebner, J.A. Ritter, Ferromagnetic seeding for the magnetic targeting of drugs and radiation in capillary beds, J. Magn. Magn. Mater. 310 (2007) 131–144, http://dx.doi.org/10.1016/j.jmmm.2006.08.009.
[23] Z.G. Forbes, B.B. Yellen, D.S. Halverson, G. Fridman, K.A. Barbee, G. Friedman, Validation of high gradient magnetic field based drug delivery to magnetizable implants under flow, IEEE Trans. Biomed. Eng. 55 (2008) 643–649, http://dx.doi.org/10.1109/TBME.2007.899347.
[24] B.B. Yellen, Z.G. Forbes, D.S. Halverson, G. Fridman, K.A. Barbee, M. Chorny, R. Levy, G. Friedman, Targeted drug delivery to magnetic implants for therapeutic applications, J. Magn. Magn. Mater. 293 (2005) 647–654, http://dx.doi.org/10.1016/j.jmmm.2005.01.083.
[25] A.D. Grief, G. Richardson, Mathematical modelling of magnetically targeted drug delivery, J. Magn. Magn. Mater. 293 (2005) 455–463, http://dx.doi.org/10.1016/j.jmmm.2005.02.040.
[26] C.W. Yung, J. Fiering, A.J. Mueller, D.E. Ingber, Micromagnetic-microfluidic blood cleansing device, Lab Chip 9 (2009) 1171–1177, http://dx.doi.org/10.1039/b816986a.
[27] S. Sanchez, A.A. Solovev, S.M. Harazim, O.G. Schmidt, Microbots swimming in the flowing streams of microfluidic channels, J. Am. Chem. Soc. 133 (2011) 701–703, http://dx.doi.org/10.1021/ja109627w.
[28] O. Rotariu, N.J.C. Strachan, Modelling magnetic carrier particle targeting in the tumor microvasculature for cancer treatment, J. Magn. Magn. Mater. 293 (2005) 639–646, http://dx.doi.org/10.1016/j.jmmm.2005.01.081.
[29] E.J. Furlani, E.P. Furlani, A model for predicting magnetic targeting of multifunctional particles in the microvasculature, J. Magn. Magn. Mater. 312 (2007) 187–193, http://dx.doi.org/10.1016/j.jmmm.2006.09.026.
[30] Institute of Electrical and Electronics Engineers, IEEE Standard for Safety Levels with Respect to Human Exposure to Electromagnetic Fields, 0–3 kHz, 2002. doi:10.1109/IEEESTD.2002.94143.
[31] C. Alexiou, R. Jurgons, R. Schmid, A. Hilpert, C. Bergemann, F. Parak, H. Iro, In vitro and in vivo investigations of targeted chemotherapy with magnetic nanoparticles, J. Magn. Magn. Mater. 293 (2005) 389–393, http://dx.doi.org/10.1016/j.jmmm.2005.02.036.
[32] A.S. Lubbe, C. Bergemann, W. Huhnt, T. Fricke, H. Riess, Predinical experiences drug targeting: tolerance and efficacy, Cancer Res. 56 (1996) 4694–4701.
[33] C. Alexiou, R. Jurgons, R. Schmid, W. Erhardt, F. Parak, C. Bergemann, H. Iro, Magnetic rug Targeting – A new approach in locoregional tumor therapy with chemotherapeutic agents. Experimental animal studies, HNO 53 (2005) 618–622, http://dx.doi.org/10.1007/s00106-004-1146-5.
[34] A. Nacev, Magnetic Drug Targeting: Developing the Basics, University of Maryland, College Park, 2013.
[35] J.B. Mathieu, S. Martel, Magnetic microparticle steering within the constraints of an MRI system: proof of concept of a novel targeting approach, Biomed. Microdevices 9 (2007) 801–808, http://dx.doi.org/10.1007/s10544-007-9092-0.
[36] N. Pekas, M. Granger, M. Tondra, A. Popple, M.D. Porter, Magnetic particle diverter in an integrated microfluidic format, J. Magn. Magn. Mater. 293 (2005) 584–588, http://dx.doi.org/10.1016/j.jmmm.2005.01.077.
[37] S. Kulkarni, B. Ramaswamy, E. Horton, S. Gangapuram, A. Nacev, D. Depireux, M. Shimoji, B. Shapiro, Quantifying the motion of magnetic particles in excised tissue: effect of particle properties and applied magnetic field, J. Magn. Magn. Mater. 393 (2015) 243–252, http://dx.doi.org/10.1016/j.jmmm.2015.05.069.
[38] K. Hournkumnuard, M. Natenapit, Magnetic drug targeting by ferromagnetic microwires implanted within blood vessels, Med. Phys. 40 (2013) 62302, http://dx.doi.org/10.1118/1.4805097.
[39] C. Alexiou, W. Arnold, P. Hulin, R.J. Klein, H. Renz, F.G. Parak, C. Bergemann, A.S. Lübbe, Magnetic mitoxantrone nanoparticle detection by histology, X-ray and MRI after magnetic tumor targeting, J. Magn. Magn. Mater. 225 (2001) 187–193, http://dx.doi.org/10.1016/S0304-8853(00)01256-7.
[40] S. Li, L. Huang, Nonviral gene therapy: promises and challenges, Gene Ther. 7 (2000) 31–34, http://dx.doi.org/10.1038/sj.gt.3301110.
[41] C.C.C.C. Berry, Progress in functionalization of magnetic nanoparticles for applications in biomedicine, J. Phys. D Appl. Phys. 198 (2009) 224003, http://dx.doi.org/10.1088/0022-3727/42/22/224003.
[42] M. Shinkai, Functional magnetic particles for medical application, J. Biosci. Bioeng. 94 (2002) 606–613, http://dx.doi.org/10.1016/S1389-1723(02)80202-X.
[43] E.M. Cherry, P.G. Maxim, J.K. Eaton, Particle size, magnetic field, and blood velocity effects on particle retention in magnetic drug targeting, Med. Phys. 37 (2010) 175–182, http://dx.doi.org/10.1118/1.3271344.
[44] M. Tehrani, J. Yoon, A novel scheme for nanoparticle steering in blood vessels using a functionalized magnetic field, Ellipsis, IEEE Trans. 62 (2015) 303–313, http://dx.doi.org/10.1109/TBME.2014.2351234.
[45] Thomas B. Jones, Electromechanics of Particles, Cambridge University Press, 1995.
[46] B. Shapiro, S. Kulkarni, A. Nacev, S. Muro, P.Y. Stepanov, I.N. Weinberg, Open challenges in magnetic drug targeting, Wiley Interdiscip. Rev. Nanomed. Nanobiotechnol. 7 (2015) 446–457, http://dx.doi.org/10.1002/wnan.1311.
[47] Ronald L. Panton, Incompressible flow, 4th ed., John Wiley & Sons, 2013, http://www.wiley.com/WileyCDA/WileyTitle/productCd-1118013433.html (accessed September 19, 2016).
[48] J.H. Leach, Magnetic targeted drug delivery, Virginia Polytechnic Institute and State University, 2003.
[49] A. Shahidian, M. Ghassemi, S. Khorasanizade, M. Abdollahzade, G. Ahmadi, Flow analysis of non-Newtonian blood in a magnetohydrodynamic pump, IEEE Trans. Magn. 45 (2009) 2667–2670, http://dx.doi.org/10.1109/TMAG.2009.2018954.
[50] D.S. Sankar, K. Hemalatha, A non-Newtonian fluid flow model for blood flow through a catheterized artery—Steady flow, Appl. Math. Model. 31 (2007) 1847–1864, http://dx.doi.org/10.1016/j.apm.2006.06.009.
[51] W.A. Seed, N.B. Wood, Velocity patterns in the aorta, Cardiovasc. Res. 5 (1971) 319–330, http://dx.doi.org/10.1093/cvrese/5.3.319.
[52] D.J. David J. Griffiths, Introduction to electrodynamics, Prentice Hall, 1999.
[53] N.C.L. Hess, D.J. Carlson, J.D. Inder, E. Jesulola, J.R. Mcfarlane, N.A. Smart, Clinically meaningful blood pressure reductions with low intensity isometric handgrip exercise. A randomized trial, 4, illustr ed., Pearson, 2016. doi:10.1017/CBO9781107415324.004.
[54] M. Kutz, Standard Handbook of Biomedical Engineering and Design, McGraw-Hill, 2003.
[55] B.R. Bacon, D.D. Stark, C.H. Park, S. Saini, E.V. Groman, P.F. Hahn, C.C. Compton, J.T. Ferrucci, Ferrite particles: a new magnetic resonance imaging contrast agent. Lack of acute or chronic hepatotoxicity after intravenous administration, J. Lab. Clin. Med 110 (1987) 164–171, http://europepmc.org/abstract/med/3598345 (accessed May 13, 2016)..
[56] M.G. Harisinghani, J. Barentsz, P.F. Hahn, W.M. Deserno, S. Tabatabaei, C.H. van de Kaa, J. de la Rosette, R. Weissleder, Noninvasive detection of clinically occult lymph-node metastases in prostate cancer, N. Engl. J. Med. 348 (2003) 2491–2499, http://dx.doi.org/10.1056/NEJMoa022749.
[57] J.B. Segur, H.E. Oberstar, Viscosity of glycerol and its aqueous solutions, Ind. Eng. Chem. 43 (1951) 2117–2120, http://dx.doi.org/10.1021/ie50501a040.